Modelling and Simulation in Materials Science and Engineering

PAPER

Computational study of ignition behavior and hotspot dynamics of a potential class of aluminized explosives

IOP Publishing Modelling and Simulation in Materials Science and Engineering
Modelling Simul. Mater. Sci. Eng. **26** (2018) 085004 (28pp) https://doi.org/10.1088/1361-651X/aae402

Computational study of ignition behavior and hotspot dynamics of a potential class of aluminized explosives

Ushasi Roy[1], Seokpum Kim[2], Christopher Miller[1], Yasuyuki Horie[3] and Min Zhou[1]

[1] The George W Woodruff School of Mechanical Engineering, School of Materials Science and Engineering, Georgia Institute of Technology, Atlanta, GA 30332-0405, United States of America
[2] Oak Ridge National Laboratory, PO Box 2008, Oak Ridge, TN 37831, United States of America
[3] (ret.) Air Force Research Lab, Munitions Directorate, 2306 Perimeter Road, Eglin AFB, FL 32542, United States of America

E-mail: min.zhou@gatech.edu

Received 1 April 2018, revised 14 September 2018
Accepted for publication 25 September 2018
Published 24 October 2018

Abstract

The ignition behavior and hotspot dynamics of a potential class of aluminized energetic materials are studied computationally. The materials consist of HMX (octahydro-1,3,5,7-tetranitro-1,3,5,7-tetrazocine) grains embedded in an aluminum matrix and, henceforth referred to as metal–matrix explosives (MMXs). For the analysis, two different MMXs, the soft MMX with a matrix of 1100 Al alloy and the hard MMX with a matrix of 7075 T651 Al alloy are considered. The thermo-mechanical response of the MMXs are computationally analyzed by subjecting them to monotonic impact loading using a Lagrangian cohesive finite element framework, with their ignition behavior analyzed through characterization of hotspots. For comparison, a polymer-bonded explosive (PBX) consisting of HMX and Estane is also analyzed under the same conditions. The results show that the MMXs have significantly lower propensity for ignition and higher structural integrity than the PBX over the loading velocity range of 200–500 m s^{-1}.

Keywords: energetic material, PBX, HMX, metal–matrix explosives, ignition, impact

(Some figures may appear in colour only in the online journal)

1. Introduction

Energetic materials (EMs) have a wide range of defense and civilian applications such as propellants, fuels, explosives, and pyrotechnics. Technical challenges include optimization with minimal trade-off among (1) performance—how to increase the energy content of EM and the delivery of power; (2) reliability—how to accurately control intended initiation/detonation and avoid accidental initiation/detonation; and how to ensure the survivability and integrity of EM against mechanical insults (e.g., impact, accidental loading)? These challenges are coupled in the sense that they all depend on the design of the materials' microstructures and changes in microstructure in general will affect all three attributes. As a result, trade-offs may have to be accepted in the development of the materials. For example, increasing the binder content may help improve the survivability, but leads to lower energy content in the overall material. The design of EM with considerations of such trade-offs to date has relied on empiricism and intuition based on numerous trial-and-error laboratory iterations. How can we systematically explore material microstructural configurations that may or may not be in existence to (1) push the envelope and provide superior all-around properties, and (2) provide attributes that can be tailored for different applications? Answers to such questions partly lies in the paradigm-shifting integrated computational materials science and engineering approach which transforms the development of EM from the historical empiricism to modeling and simulation based design science that accounts for microstructural characteristics, constituent properties, processing, and loading conditions the materials are subjected to in application. As part of this approach, computational materials design (CMD) can reduce the time and cost of development and bring about advanced materials with properties tailored according to specific performance requirements. CMD through modeling and simulation not only allows assessment of existing materials but also permits exploration of material configurations not yet in existence.

CMD requires recognition of the multiscale (nano, micro, meso and macro) and multiphysics (thermal, mechanical and chemical) nature (Baer 2002, Horie 2014) of the processes that govern the responses of EMs. The multiscale nature of the problem manifests not only in the nano-to-macro size hierarchy of material structural heterogeneities, but also in time because loading (shock, non-shock) and physical processes (mechanical, thermal and chemical) span times from nanoseconds to milliseconds. Solutions to the problem should also address the stochastic nature of the ignition of EM due to the heterogeneous nature of the materials. The microstructure scale (or mesoscale, as it is often referred to as) for polymer-bonded explosives (PBXs) concerns material heterogeneities on the order of microns to hundreds of microns (μm). It is at this scale that materials processing and synthesis have one of the most significant influences on material structural hierarchy—for a given combination of constituents and composition. Naturally, this scale is one of the focuses of materials design and engineering, both experimentally and computationally (Baer 2002, Gonthier 2003, Foster *et al* 2007, Trott *et al* 2007, Barua and Zhou 2011b, Panchadhara and Gonthier 2011, Gilbert and Gonthier 2012, Barua *et al* 2012a, 2012b, 2013a, 2013b). Materials design must be coupled with materials fabrication in order for new materials to be developed. In addition to traditional fabrication processes, additive manufacturing (AM) allows flexible and cost-effective fabrication of innovative and complex materials (Lewis 2006). Additively manufactured energetic materials with customized/graded solid loadings of explosive crystals, metals, thermites, or biocidal/chemicidal additives have been developed since the 1980s (Daniel 2006, Guo and Leu 2013, Ruzz-Nuglo 2014, Schrand 2016). The advent of AM provides a unique opportunity for realizing computationally designed materials and iterative improvement of the material design. It is under this setting that we carry out the current

computation on an exploratory class of materials that may not be in existence at the moment. In order to explore the ignition behavior of a novel class of heterogeneous energetic material (HEM), we choose the size scale on the order of mm to tens of mm (microstructure scale) and the time scale on the order of microseconds for our computations.

Solid high explosives like HMX (octahydro-1,3,5,7-tetranitro-1,3,5,7-tetrazocine) and RDX (1,3,5-trinitroperhydro-1,3,5-triazine) are powerful sources of energy for propulsion as well as civilian and military applications. They have high energy densities which are on the order of 1 kcal g^{-1}. Their combustion can lead to detonations that propagate at speeds of 7–9 km s^{-1} and release energy at rates up to 100 GW cm^{-2} (Asay 2010, Barua and Zhou 2011b). The ignition sensitivity of such EMs is of great importance as even improper handling of these materials can lead to disasters, including the loss of properties and human lives. Unfortunately, history is full of such events. Therefore, a continuous quest exists to design safer EMs which will only ignite under stringent conditions and can minimize accidental detonations. One effective approach to modify the ignition behavior of such materials is to embed them in a polymer binder to form composites known as PBXs. To further alter the energy content and reaction behavior of these composites, aluminum is often added.

Dahmen (1904) first introduced Al to systems of explosives for better performance. Since then, the aluminization of explosives has been studied extensively (Dahmen 1904, Brousseau *et al* 2002, Rumchik *et al* 2007, Trzciński *et al* 2007). Aluminum has been added to almost all EMs, including those containing HMX, RDX, TNT, and PETN. Aluminization decreases the velocity of detonation and increases the heat of reaction almost without exception. For instance, a 25% of Al in HMX by volume reduces the velocity of detonation from 8.76 to 7.97 km s^{-1}. The heat of explosion increases from 5389 to 5927 kJ kg^{-1} when 10% of Al is added to an EM consisting of RDX, TNT, and wax. In such cases, Al serves as a metallic fuel, adding to the heat of explosion. Kim *et al* (2014) showed through computational simulations that Al desensitizes an HMX-based PBX, consistent with experimental observations (Radwan 2001, Prakash *et al* 2004). This fact, along with the fact that embedding energetic granules in a matrix can make explosives safer to handle, gives rise to the concept of a potential novel EM system formed by replacing the polymer binder in PBX with Al, which can enhance heat of reaction and have a wider range of mechanical strength and better thermal stability than polymers and, therefore, can lead to better mechanical integrity and thermal stability of the overall energetic composite. There may be other benefits as well. For example, the electrical conductivity of an Al matrix can lend an EM to rapid simultaneous large-scale detonation by microwave or electrical impulse at multiple locations via the use of, e.g., electrical bridge wires, a benefit non-conductive PBXs do not offer. Removing polymer from PBX would also eliminate aging as a concern and give longer life and better thermal and vibratory stability to the EM. However, at this time, it is not clear how a metal (Al) matrix EM or metal–matrix explosive (MMX) would be made. In the paper, we computationally analyze the response of MMXs to dynamic loading in an effort that can be considered as computational design and exploration of a class of materials that are not yet in existence.

Hardin (2015) first performed a systematic numerical study on the hotspot dynamics of HEMs with Al alloys as matrix in place of Estane in a PBX. They named the new system of HEM as aluminum-bonded explosives. To circumvent the issue of bonding and focus on the issue of response, we believe these materials can be more appropriately called MMXs as explained earlier. In this study, Al alloys are used as the matrix metal to carry out the thought experiment and computationally predict the performance of such an MMX system. For this exploratory study, we focus on analyzing the potential benefits in terms of ignition behavior alone and will not address the issue of how the materials can be made, noting that vacuum arc melting, evaporation, or AM are possibilities. From a materials development perspective, we

consider this analysis as the first step to design a new material system. Fabrication can come later, if such materials are found to be desirable or have superior attributes.

Hotspot formation plays an important role in determining the ignition initiation of HEM. By initiation, we mean the attainment of the criticality condition that sets the chemical reaction on a self-sustained path that leads to ultimate detonation. Detonation is an outcome following ignition initiated at the hotspots and we explore the generation and initiation of these hotspots rather than how initiation transitions into detonation. In particular, the size, temperature, and rate of development of the hotspots are important. To quantify the relationship between these parameters, loading, and material microstructure, Barua *et al* (Barua and Zhou 2011a, 2011b, Barua *et al* 2012a, 2012b) developed a computational framework based on the cohesive finite element method (CFEM) that enables the establishment of microstructure—performance relations for heterogeneous EMs through mesoscale simulations that account for coupled thermal-mechanical processes that dominate the response of EM under dynamic loading. Specifically, this novel framework and associated software suite Cohesive Dynamics for Explosives (CODEX) account for most of the important physical processes dominating the thermo-mechanical response of EM under mechanical or thermo-mechanical insults. Factors considered include arbitrary microstructural morphologies and arbitrary combinations of constituents; large elastic, elastoviscoplastic, and viscoelastic deformations; heat generation and conduction; thermal softening; strain rate sensitivity; coupling of the thermal and mechanical processes; fracture, damage, friction; and frictional heating along crack surfaces. This framework has been further developed and used in the analysis reported here. The analysis carried out accounts for statistical variations in material microstructural heterogeneity which is the primary source of stochastic variations in the ignition behavior and the hotspot dynamics that determine the ignition response (Barua *et al* 2013a, 2013b) of the materials. The focus is on both the hotspot dynamics and ignition response.

2. Framework of analysis

2.1. Material

The particular PBX that serves as the starting point and reference material of the analysis has HMX grains in an Estane 5703 matrix. The MMXs are configured by replacing the polymer in the PBX with Al alloys. These alloys differ from Estane primarily in their constitutive behavior. Different grades of Al alloys are known to follow elastoviscoplastic constitutive behavior with a wide range of strength and ductility, while Estane shows viscoelastic response to mechanical loading. Commercially pure 1100 Al alloy possesses higher strength and ductility than those of Estane but is softer compared to the aircraft grade 7075 T651 Al alloy. The latter is widely used as a high strength structural material. Therefore, these two alloys with widely varying strength and toughness levels are chosen for this study to explore the effect of mechanical response of the matrix on the deformation and ignition behavior of the MMX subject to mechanical insults. The MMX having 1100 Al alloy is thus referred to as the 'soft' MMX and the one with 7075 T651 Al alloy is referred to as the 'hard' MMX. All three materials considered here contain ∼81% HMX by volume, with the rest of the volume occupied by the matrix. Voronoi tessellation (Ghosh *et al* 1997, Kim *et al* 2016) is used to generate 2D microstructures that have multifaceted HMX grains with monomodal distribution of sizes (figures 1 and 2). Voronoi tessellation is an approach for the subdivision of a region via the use of a set of points, such that each point has associated with it a region that is closer to it than to any other point. These regions are termed Voronoi cells and may be identified as

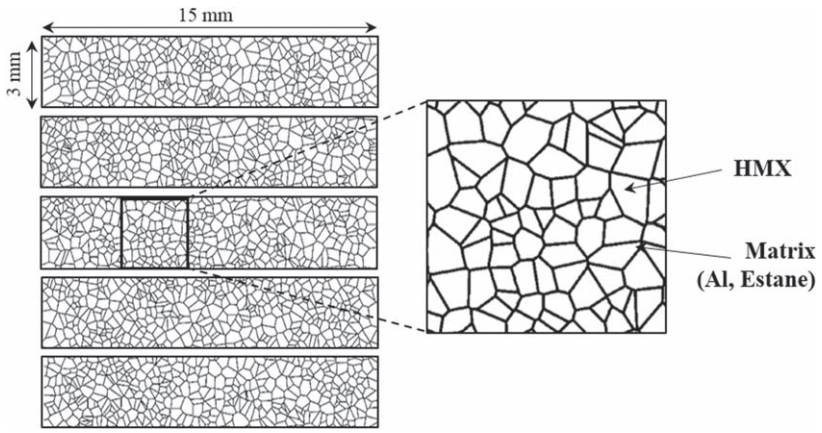

Figure 1. Computationally generated, statistically similar instantiations of microstructures with monomodal grain size distribution and a grain fraction of 0.81. A total of 20 instantiations are used, five of which are shown here.

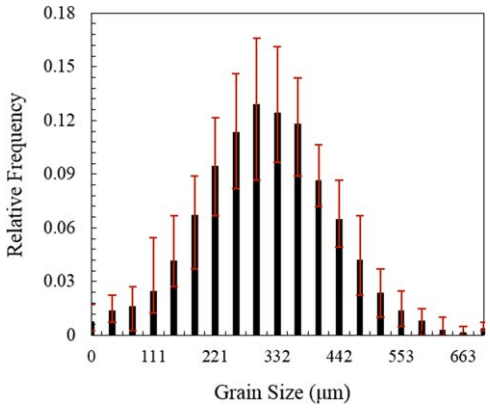

Figure 2. Size distribution of HMX grains in the computationally generated microstructures. The average grain size (d_{avg}) is 310 $\pm$ 119 μm and the grain fraction is 0.81.

the basic structural elements of a heterogeneous microstructure. Polycrystalline microstructures generated using Voronoi tessellation has multifaceted grains interlocked with each other. In our analysis, frictional dissipation along crack surfaces is an important mechanism of hotspot generation, hence we prefer the well-defined grain structure generated by Voronoi tessellation. Another benefit of Voronoi tessellation is that it allows convenient generation of sets of microstructures with statistically equivalent attributes. In this work, the average grain size is 310 μm. For systematic quantification of the probabilistic ignition behavior, statistically similar sample sets with multiple instantiations are generated and analyzed under identical loading conditions. Figure 1 shows five examples of twenty such random instantiations of statistically similar microstructures used in the analysis.

In order to model the mechanical behavior of the microstructural constituents, elasto-viscoplastic constitutive laws are used for both the HMX grains and the Al alloys. For Estane, a generalized viscoelastic Maxwell model is adopted, as described in Barua and

Zhou (2011b). A brief outline of the constitutive and interfacial relations is given below (Zhou *et al* 1994).

The deviatoric part of the constitutive behavior of HMX grains and Al matrix is described by an elastoviscoplastic model. The specific form of the constitutive relation used is

$$\hat{\boldsymbol{\tau}}' = \mathbf{L}\colon (\mathbf{D}' - \mathbf{D}'_{\mathbf{p}}), \tag{1}$$

where $\mathbf{L}$ is the tensor of elastic moduli, $\hat{\boldsymbol{\tau}}'$ is the deviatoric part of the Jaumann rate of the Kirchhoff stress, and $\mathbf{D}'$ is the deviatoric part of the rate of deformation. For isotropic elastic response,

$$\mathbf{L} = 2\mu\tilde{\mathbf{I}} + \lambda\mathbf{I} \otimes \mathbf{I}. \tag{2}$$

Here, $\tilde{\mathbf{I}}$ is the fourth order identity tensor, λ and μ are Lamé's first and second constants. $\mathbf{D}'$ in equation (1) can be decomposed into an elastic part and a viscoplastic part as

$$\mathbf{D}' = \mathbf{D}'_{\mathbf{e}} + \mathbf{D}'_{\mathbf{p}}, \tag{3}$$

where $\mathbf{D}'_{\mathbf{p}}$ is the viscoplastic part of $\mathbf{D}'$ in the form of

$$\mathbf{D}'_{\mathbf{p}} = \frac{3\dot{\bar{\varepsilon}}}{2\bar{\sigma}}\boldsymbol{\tau}', \text{ with } \bar{\sigma}^2 = \frac{3}{2}\boldsymbol{\tau}'\colon \boldsymbol{\tau}'. \tag{4}$$

In the above relations, $\bar{\sigma}$ is the Mises equivalent stress, $\boldsymbol{\tau}'$ is the deviatoric part of the Kirchhoff stress, and $\dot{\bar{\varepsilon}}$ is the equivalent plastic strain rate which has the form of

$$\left.\begin{aligned} \dot{\bar{\varepsilon}} &= \frac{\dot{\bar{\varepsilon}}_1\dot{\bar{\varepsilon}}_2}{\dot{\bar{\varepsilon}}_1 + \dot{\bar{\varepsilon}}_2}, \\ \dot{\bar{\varepsilon}}_1 &= \dot{\bar{\varepsilon}}_0\left[\frac{\bar{\sigma}}{g(\bar{\varepsilon}, T)}\right]^m, \\ \dot{\bar{\varepsilon}}_2 &= \dot{\bar{\varepsilon}}_m \exp\left[-\frac{a\, g(\bar{\varepsilon}, T)}{\bar{\sigma}}\right], \\ g(\bar{\varepsilon}, T) &= \sigma_0\left(1 + \frac{\bar{\varepsilon}}{\varepsilon_0}\right)^N\left\{1 - \beta\left[\left(\frac{T}{T_0}\right)^\kappa - 1\right]\right\}, \end{aligned}\right\} \tag{5}$$

where $\bar{\varepsilon} = \int_0^t \dot{\bar{\varepsilon}}\mathrm{d}t$ is the equivalent plastic strain, $\dot{\bar{\varepsilon}}_0$ and $\dot{\bar{\varepsilon}}_m$ are reference strain rates, m and a are rate sensitivity parameters for strain rates below $10^3\ \mathrm{s}^{-1}$ and above $5 \times 10^4\ \mathrm{s}^{-1}$ respectively, σ_0 is the quasi-static yield stress, ε_0 is a reference strain, N is the strain hardening exponent, T_0 is a reference temperature, and β and κ are thermal softening parameters. The function $g(\bar{\varepsilon}, T)$ represents the quasi-static stress–strain response at ambient temperature. The above relations consider strain hardening and strain rate dependence of plasticity. The details of the above constitutive relations and descriptions of the parameters can be found in the literature (Zhou *et al* 1994). The values of the parameters for HMX used in this study are listed in table 1. The difference between computationally generated microstructures and the experimental microstructures is the presence of voids. Experimentally observed voids are too small to be resolved explicitly via finite element meshing at the overall size scale of sample analyzed. Another way to look at this is that the time scale for voids to fully collapse is a few nanoseconds, much shorter than the time scale of several microseconds of our simulations at the microstructure level here. Also, Rai *et al* (2017a, 2017b) showed that void collapse does not contribute to hotspots formation when the applied impact velocity is below $500\ \mathrm{m\,s}^{-1}$ and the presence of voids softens the bulk material behavior to some extent. Therefore, the effect

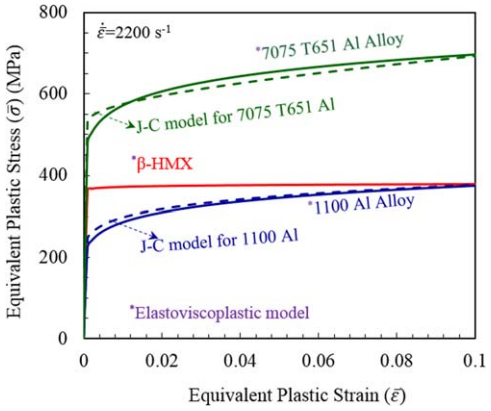

Figure 3. Stress–strain curves for β-HMX, 1100 Al alloy and 7075 T651 Al alloy. The elastoviscoplastic model for the Al alloys are compared with the corresponding Johnson–Cook models in the literature (Brousseau *et al* 2002, Vadhe *et al* 2008).

Table 1. Properties of HMX, 1100 Al and 7075 T651 Al alloy.

Material properties	HMX	1100 Al alloy	7075 T651 Al alloy
E (MPa)	21.20	65.76	71.70
ϑ	0.277	0.33	0.33
ρ (g cm^{-3})	1.91	2.80	2.80
σ_0 (MPa)	260	148.36	527
ε_0	5.88×10^{-4}	1.6×10^{-2}	1.6×10^{-2}
N	0.0	0.11	0.08
T_0 (K)	300	293	292
β	0.0	2.7	2.7
$\bar{\varepsilon}_0$	1×10^{-4}	5×10^{-4}	5×10^{-4}
m	100.0	70	125
$\bar{\varepsilon}_m$	8×10^{-4}	8×10^{12}	8×10^{10}
α	22.5	30.0	5.0
κ	3.0	3.0	3.0

of voids is incorporated phenomenologically in the material constitutive model. The parameters of the material model for HMX are calibrated to match the experimental wave profile obtained by Dick *et al* (2004). The verification of the calibrated parameters is described in literature (Hudson *et al* 2012, Hardin 2015). Since the magnitudes of parameters used to describe the elastic-viscoplastic constitutive equations are calibrated and verified with experimental results on real HMX, the constitutive model takes into account the overall effect of voids and defects on the mechanical response of HMX. The equivalent stress–strain response of the constituents as calculated from the models at the strain rate of 2200 s^{-1} is shown in figure 3. The figure suggests HMX assumes a non-hardening elastoviscoplastic behavior. The elastoviscoplastic model used here for 1100 and 7075 T651 Al alloys are compared with the well-established Johnson–Cook model (Brar *et al* 2009, Iqbal *et al* 2010) as shown in figure 3. In both cases, the two models match each other well.

The volumetric part of the response is described by the Birch–Murnaghan equation of state (B–M EOS). The specific form of the equation is

$$\tau_h = \frac{3}{2}K_0\left(\frac{\mathrm{d}V}{\mathrm{d}V_0}\right)\left\{\left(\frac{\mathrm{d}V}{\mathrm{d}V_0}\right)^{-\frac{7}{3}} - \left(\frac{\mathrm{d}V}{\mathrm{d}V_0}\right)^{-\frac{5}{3}}\right\}\left[1 + \frac{3}{4}(K_0' - 4)\left\{\left(\frac{\mathrm{d}V}{\mathrm{d}V_0}\right)^{-\frac{2}{3}} - 1\right\}\right], \tag{6}$$

where $\tau_h = \tau_{ii} = \tau_{11} + \tau_{22} + \tau_{33}$ is the hydrostatic part of the Kirchoff stress which is the product of the Jacobian and the negative of the hydrostatic pressure. K_0 is the bulk modulus, and $K_0' = (\partial K_0/\partial P)_{P=0}$. $\mathrm{d}V/\mathrm{d}V_0$ is the volume ratio of an initial volume element ($\mathrm{d}V_0$) and the current volume element, which is equal to the Jacobian ($J = \det(\mathbf{F})$ with $\mathbf{F}$ being the deformation gradient). For the implementation of the B–M EOS, a time incremental form is used. The time rate of change of the Jacobian is

$$\frac{\partial}{\partial t}\left(\frac{\mathrm{d}V}{\mathrm{d}V_0}\right) = \left(\frac{\mathrm{d}V}{\mathrm{d}V_0}\right)\mathrm{tr}(\mathbf{D}), \tag{7}$$

and the rate of change of the hydrostatic Kirchhoff stress is a function of the Jacobian and rate of deformation, i.e.,

$$\frac{\partial \tau_h}{\partial t} = f\left(\frac{\mathrm{d}V}{\mathrm{d}V_0}, \mathrm{tr}(\mathbf{D})\right). \tag{8}$$

The parameter values used in this study are $K_0 = 16.71$ GPa and $K_0' = 7.79$ for HMX (Landerville *et al* 2010), and $K_0 = 72.7$ GPa and $K_0' = 4.14$ for the aluminum alloys (Ahmad and Alkammash 2012).Interfacial debonding and arbitrary fracture patterns are explicitly captured by the use of cohesive elements embedded throughout the finite element model, along all finite element boundaries. The cohesive elements follow a bilinear traction separation law described by Zhai *et al* (2004). In this cohesive model, the traction applied on any cohesive surface ($\mathbf{T}$) is work conjugate to the interfacial separation ($\mathbf{\Delta}$). This law is derived from a potential, Φ, which is related to $\mathbf{\Delta}$ through the state variable

$$\lambda = \begin{cases} \sqrt{\left(\dfrac{\Delta_n}{\Delta_{nc}}\right)^2 + \left(\dfrac{\Delta_t}{\Delta_{tc}}\right)^2}, & \Delta_n \geqslant 0; \\ \left|\dfrac{\Delta_t}{\Delta_{tc}}\right|, & \Delta_n < 0; \end{cases}, \tag{9}$$

where $\Delta_n = \mathbf{n}\cdot\mathbf{\Delta}$ and $\Delta_t = \mathbf{t}\cdot\mathbf{\Delta}$ are the normal and tangential components of $\mathbf{\Delta}$, respectively, and $\mathbf{n}$ and $\mathbf{t}$ are the unit vectors normal and tangential to the cohesive surface. Δ_{nc} and Δ_{tc} are the critical normal and shear separations at which the cohesive strength vanishes and the cohesive element fails. This state variable describes the effective state of the cohesive element under mixed-mode separations. To capture the irreversibility of damage, the monotonically increasing parameter $\eta = \max(\eta_0, \lambda_{\mathrm{ul}})$ is introduced. η_0 is the initial value of η which describes the initial slope $(1/\eta_0)$ of the normalized/non-dimensional ($\sigma/T_{\max}$ versus λ) cohesive relation in figure 4. Also, λ_{ul} is the maximum value of λ experienced by the element at the onset of an unloading event. Thus, $1/\lambda_{\mathrm{ul}}$ represents the reduced slope of the normalized cohesive relation after damage and unloading have occurred. The limiting values of $\lambda = 0$ and $\lambda = 1$ correspond to zero separation and complete element degradation, respectively. As shown in the figure 4, between points A and B, separation occurs elastically and the work done is fully recoverable. Between points B and C, material degradation causes progressive reduction in the cohesive strength and thus the cohesive law phenomenologically takes into account the effect of microcracks and other defects, not explicitly modeled in the current set-up. Unloading from any point P follows path PA and

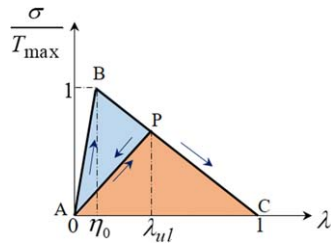

Figure 4. Bilinear traction separation law for the cohesive elements.

subsequent reloading follows path AP and then PC. The hysteresis loop ABP depicts the dissipation during the softening process. Stress (σ) at the cohesive surfaces is defined as

$$\sigma = \sqrt{(T_n)^2 + (T_t/\alpha)^2} = \begin{cases} \left(T_{\max}\dfrac{1-\eta}{1-\eta_0}\right)\dfrac{\lambda}{\eta}, & 0 \leqslant \lambda \leqslant \eta \\ \left(T_{\max}\dfrac{1-\eta}{1-\eta_0}\right)\dfrac{1-\lambda}{1-\eta}, & \eta < \lambda \leqslant 1 \\ 0, & \lambda > 1, \end{cases} \tag{10}$$

where $\alpha = \Delta_{nc}/\Delta_{tc}$. T_n and T_t represent the normal and tangential components of the traction applied on a cohesive surface.

The work of separation, strength of cohesion, and separation distance at which the interface loses all traction-carrying capability relate to the fracture toughness of the material. Therefore, the values of these cohesive parameters are different for different types of materials and interfaces. These parameters are calibrated using available data in the literature. The cohesive finite element framework explicitly captures different fracture mechanisms including interfacial debonding. A verification of the cohesive element framework is provided by Barua and Zhou (2011b). In order to resolve the issue of one bulk element penetrating into another after the adjoining cohesive elements fail, a multi-step contact algorithm is used. Detailed descriptions of the multi-step contact algorithm which includes calculations of penetration depth and surface traction are given by Hardin (2015). We apply penalty forces to the contacting surfaces to strongly discourage or prevent interpenetration. The tangential component of the applied penalty force depends upon friction between the contacting surfaces. The friction algorithm is based on the Coulomb friction model. The magnitude of frictional force depends upon the coefficient of friction. We determine the relative sliding of the cracked surfaces under the applied frictional force in order to determine the frictional work of contact. This frictional work of contact is converted into heat, resulting in local heating.

The temperature in the material under dynamic loading rises locally not only due to frictional dissipation along the interfaces but also due to inelastic bulk dissipation. Therefore, heat conduction is considered. The specific form of the heat equation is

$$\rho c_v \frac{\partial T}{\partial t} = k\nabla^2 T + \eta \dot{W}^p + \dot{W}^{\text{fric}}, \tag{11}$$

where ρ is density, c_v is specific heat, T is temperature, t is time, k is thermal conductivity, η is the fraction of plastic work that is converted into heat, $\dot{W}^p$ is the rate of plastic work, and $\dot{W}^{\text{fric}}$ is the rate of frictional dissipation. The rate of plastic work depends upon the bulk material models, whereas, the rate of frictional dissipation depends upon the coefficient of friction as

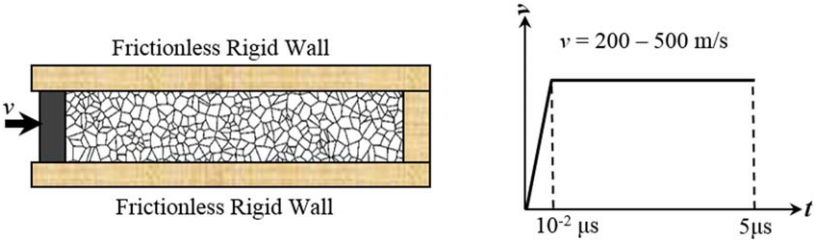

Figure 5. Configuration of the computational model along with the loading and boundary conditions.

Table 2. Cohesive parameters for the grains and the matrices.

Parameters	HMX	Estane	1100 Al	7075 T6 Al
Δ_{nc} (μm)	5.00	10.00	15.40	27.90
Δ_{nc}/Δ_{tc}	1	1	1	1
η_0	0.01	0.001	0.046	0.02
$T_{\max}$ (MPa)	101	38.4	345.5	570

mentioned earlier. Green *et al* (1971) experimentally estimated the magnitude of the coefficient of friction for an HMX-based PBX to be 0.3–0.7. Chidester *et al* (1993) used the value of 0.5 as the coefficient of friction to model frictional dissipation and consequent hotspots formation for another HMX-based PBX specimen. Another work by Dickson *et al* (2006) finds that the coefficient of friction for PBX 9501 varies between 0.35 and 0.5. Barua (2013) showed that in the range of 0.5–0.7, the frictional dissipation increases by only 3%. We have used the value of 0.5 for all our calculations.

2.2. Loading configuration

The specimens are 15 mm $\times$ 3 mm in dimensions and are subjected to loading under a macroscopically uniaxial state of strain as shown in figure 5. Since the dimensions of the specimens are small compared to the size of some macroscopic applications and only representative cells of the overall material, the lateral sides of the specimens are confined by frictionless rigid walls to effect the conditions of overall uniaxial strain. This handling allows analyses of material behavior at higher scales without the effects of rarefaction waves from finite sample boundaries or free surfaces. Loading is effected through the imposition of a piston velocity (v) at the left end of the sample which ranges from 200 to 500 m s^{-1} for a duration of 5 μs. The boundary velocity is increased from 0 to its maximum value (200, 300, 400, and 500 m s^{-1}) over a ramping period of 10 ns as shown in the figure. The initial temperature is 300 K for all the calculations presented here.

2.3. Computational approach

The Lagrangian CFEM framework of Barua *et al* (Barua and Zhou 2011b) is used. This framework takes into account finite deformation, thermo-mechanical coupling, fracture in terms of random crack propagation and frictional heating. The cohesive parameters used for the constituents are listed in tables 2 and 3. These parameters are chosen based on the fracture toughness of the respective materials. For the Al-HMX interfaces, the parameters are assumed

Table 3. Cohesive parameters for the grain/matrix interfaces.

Parameters	Estane/HMX	1100 Al/HMX	7075 T6 Al/HMX
Δ_{nc} (μm)	4.62	10.20	16.45
Δ_{nc}/Δ_{tc}	1	1	1
η_0	0.049	0.035	0.015
$T_{\max}$ (MPa)	35	223	335

to take the average values of the cohesive parameters for HMX and Al alloys. The cohesive parameters for HMX, Estane, and the HMX–Estane interfaces are taken from Barua and Zhou (2011b).

2.4. Ignition analysis

The ignition behavior of the materials is characterized based on the criterion for ignition developed by Barua *et al* (2013a, 2013b). This criterion links hotspots' size–temperature states in a loading event to the threshold size–temperature conditions for hotspots (Tarver *et al* 1996) which are regarded as material properties. The details of this criterion are described in Barua *et al* (2013a). The criterion, along with the CFEM capability to quantify the thermo-mechanical behavior of EMs, allows the time to criticality (t_c) and threshold impact velocity (v_c) for ignition to be determined as functions of material composition, microstructure and loading conditions (Barua *et al* 2013a).

Mathematically, this criterion can be stated as

$$d(T) \geqslant d_c(T), \tag{12}$$

where d is the diameter of a hotspot resulting from a loading event whose interior temperatures are at or above the temperature T and d_c is the minimal diameter of a hotspot required for thermal runaway at that temperature T. The information regarding the right-hand side of equation (12) comes from Tarver *et al* (1996), who performed chemical kinetics calculations to analyze the criticality issue for HMX and TATB explosives. The calculations consider multi-step reaction mechanisms and the pressure and temperature dependence of reactants and products.

In their analysis, Tarver *et al* initially did not consider the presence of a matrix phase in the material, i.e., what they studied is hotspots in uniform, single-phase HMX or TATB. A question arises as to whether the presence of a second phase, or the fact that HMX or TATB is in contact with another material, affects the size–temperature threshold for a particular EM. This question is especially more important for Al than for polymers since metals are much more thermally conductive and, therefore, are likely to significantly influence the threshold size–temperature relation for critical hotspots. To address this issue, Dr Kim carried out an analysis using a finite difference method (FDM). In the analysis, Al is the matrix material surrounding an HMX grain. The HMX undergoes the four-step decomposition described by Tarver and Tran (2004). The sequence is as follows. First, β-HMX (A) transforms to δ-HMX (B), followed by the subsequent formation of solid intermediates (C), both through endothermic reactions. The solid intermediates transform to gaseous intermediates (D) and finally to gas (E) in two consecutive exothermic steps. The four steps can be denoted as follows,

$$A \underset{(1)}{\longrightarrow} B \underset{(2)}{\longrightarrow} C \underset{(3)}{\longrightarrow} D \underset{(4)}{\longrightarrow} E.$$

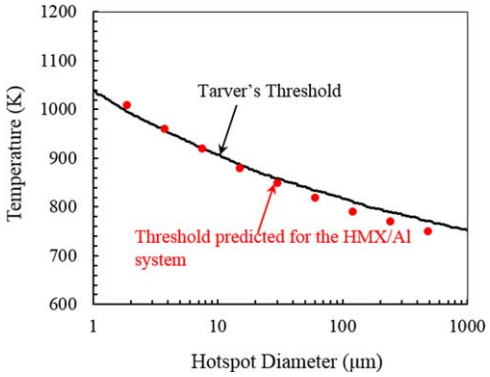

Figure 6. Hotspot size–temperature threshold for plain HMX and HMX in the HMX/Al composite. The curve for plain HMX is from Tarver *et al* (1996). The data points for the HMX in the composite are calculated using the coupled chemical kinetics and thermal conduction model of Tarver *et al.*

Table 4. Reaction kinetics parameters (Tarver and Tran 2004).

Reaction	ln$Z$	E (kcal mol^{-1})	Reaction order	q (cal g^{-1})
1	48.13	48.47	1	+10.0
2	48.7	52.7	1	+60
3	37.8	44.3	1	−133
4	28.1	34.1	2	−1337

The rate of heat generation due to chemical reaction is dictated by the order of the reaction. The first and fourth reactions shown above follow the first and second order reaction kinetics, respectively. The heat generation rates due to these reactions are given as

$$\frac{\mathrm{d}Q_1}{\mathrm{d}t} = q_1 k_1 [A] = q_1 Z_1 \mathrm{e}^{-E_1/RT}[A], \tag{13}$$

and

$$\frac{\mathrm{d}Q_4}{\mathrm{d}t} = q_4 k_4 [B]^2 = q_4 Z_4 \mathrm{e}^{-E_4/RT}[B]^2, \tag{14}$$

respectively. In the above relations, k_1 and k_4 are the reaction rate constants for the first and fourth reactions, respectively. These rate constants depend on temperature through the well-known Arrhenius equation. q_1 and q_4 are the values of heat of reaction 1 and 4 respectively. The values of these reaction kinetics parameters are taken from the literature (Tarver and Tran 2004) and are shown in table 4. The heat generation due to chemical reaction in one cell is coupled with heat from surrounding cells in the FDM framework through thermal conduction, allowing the temperature field in a hotspot to be evaluated as function of time.

Simulations are carried out for various combinations of hotspot size and initial hotspot temperature. It is observed that the threshold curve for the HMX-Al system falls very close to that of single-phase HMX as determined by Tarver *et al* (1996) (figure 6). The thermal conductivity of Estane is much lower than that of HMX or Al, making it much less likely to influence the threshold curve for HMX. Therefore, the temperature-size threshold curve for

hotspots in HMX is essentially unaffected by the matrix materials considered here and the Tarver's threshold is used to characterize the ignition behavior of the MMXs and the PBX.

To identify hotspots, a scheme developed by Barua *et al* (2013a) is used. This approach involves the use of a temperature threshold (T_{thres}). At each time step, the microstructure is scanned for temperatures above T_{thres}. Areas with temperatures above the threshold are considered as hotspots. For criticality of hotspots, Tarver's criterion is used as mentioned earlier. Left-hand side of the equation (10) is obtained by analyzing the hotspot distributions from the CFEM calculations. To account for the variation of temperature within a hotspot (note that temperatures at different spatial locations within a hotspot are different and T_{thres} is the lowest temperature at the periphery), Tarver *et al*'s criterion is stated as a band of $\pm 10\%$ about the mean value. A hotspot is considered to be critical when it crosses the critical threshold limit. Relative position of a hotspot with respect to the critical threshold line determines the risk of ignition for that hotspot. The risk factor (R) for a particular hotspot of size d and temperature T is defined as Kim *et al* (2016),

$$R = \frac{T - T_i}{T_c - T_i}, \tag{15}$$

where T_c is the critical threshold temperature for that hotspot and T_i is the initial temperature. The hotspots with R values greater than 1 (implying $T \geqslant T_c$) are deemed critical as they cross the critical threshold line for ignition.

Taking into consideration the stochastic nature of arbitrary microstructures, Barua *et al* (2013a, 2013b) employed an approach to identify the time each specimen takes to reach criticality (t_c) measured from the onset of dynamic loading. In this approach, a specimen is regarded as reaching criticality if the critical hotspot density reaches a level equal to or greater than 0.22 mm^{-2}. This level corresponds to two critical hotspots in a 3 mm^2 domain. The hotspot density criterion for criticality aids in executing a statistical analysis based on 'go'/'no-go' status of the specimen. Although, the particular critical hotspot density value appears somewhat arbitrary, it is worth pointing out that the outcome of the threshold analysis is not strongly dependent on the value, as hotspots develop quickly and simultaneously near the ignition threshold. Each of the 20 statistically similar instantiations of a material is subjected to this 'go'/'no-go' analysis. Probability distribution curves are further constructed based on the fraction of similar instantiations that reaches criticality (goes off) at a particular level of impact velocity. This cumulative probability of ignition for each material at a specific loading condition is fitted with three-parameters Weibull distribution function after Barua *et al* (2013b). The Weibull distribution function takes the form of

$$P(t) = 1 - \mathrm{e}^{-\Phi(t)}, \quad \Phi(t) = \begin{cases} 0, & t < t_0, \\ \left(\dfrac{t - t_0}{\tau}\right)^m & t \geqslant t_0, \end{cases} \tag{16}$$

where $P(t)$ is the cumulative probability, t is the time to criticality, t_0 is the cutoff or threshold time below which the probability of ignition is zero, τ is the scale parameter which affects the slope of the distribution curve and m is the shape parameter. The three parameters (τ, m, and t_0) vary with material properties and loading conditions. The median (t_{50}) of this distribution indicates the time corresponding to 50% probability of ignition. This median time to criticality (t_{50}) is considered as a parameter that quantifies the propensity for ignition. Moreover, the scale parameter τ is used to estimate the critical loading velocity below which no ignition occurs. Specifically, the plot of $1/\tau$ versus v (impact velocity) for a particular material is extrapolated to $1/\tau = 0$ to estimate the critical loading velocity (v_c) below which no ignition occurs. Details of this approach can be found in the literature (Barua *et al* 2013a).

3. Results

The results of the CFEM calculations and the subsequent ignition analyses are discussed in this section. The ignition behaviors of all three materials subjected to the same sets of loading conditions are compared in order to understand the effect of metallic matrix on their hotspot dynamics. In particular, systematic comparisons are made in terms of temperature evolution, R values, median times to criticality (t_{50}), and threshold velocities (v_c) that quantify the propensity for ignition. Comparisons are also made in terms of stress distribution, damage evolution, and energy dissipation as they govern the hotspot dynamics of mechanically loaded specimens.

3.1. Ignition behavior and hotspot dynamics

3.1.1. Effect of metallic matrix on hotspot formation. The spatial distribution of temperatures at any instant of loading indicates the extent of localized heating in the material. Figure 7 shows such temperature distributions at $t = 1$ μs in all three materials subjected to loading at two piston velocities. For an impact velocity of 200 m s^{-1}, neither MMX shows regions of localized heating where the temperature is above 400 K (T_{thres}). Hence, no hotspot forms in the MMXs after 1 μs of loading. On the other hand, hotspots are found in the PBX at the same instant. At a loading velocity of 500 m s^{-1}, temperatures in the hotspots reach 600–700 K in the PBX but are clearly lower in the hotspots in the MMXs. Specifically, while the soft MMX exhibits many hotspots with high temperatures, the overall number is lower than that in the PBX. The hard MMX exhibits far fewer hotspots and all have significantly lower temperatures as well.

3.1.2. Criticality of hotspots and risk factor. The size–temperature states of hotspots at different instants of loading are compared with Tarver's threshold line to determine the criticality of hotspots and their ignition risk factors. After 1 μs of loading at a piston velocity of 200 m s^{-1}, hotspots begin to appear in the PBX. Figure 8(a) shows size–temperature states of hotspots at an instant of 1 μs from multiple statistically similar instantiations of the PBX. The hotspots lie far away from Tarver's line, indicating improbability of ignition at 1 μs. At 2.75 μs, hotspots in significant numbers approach Tarver's line and some of them even cross the line (figure 8(b)). On the other hand, few hotspots are found in the MMXs at the velocity of 200 m s^{-1} at any instant of time, and no critical hotspots are seen. However, at a piston velocity of 500 m s^{-1}, a considerable fraction of hotspots crosses the threshold line at $t = 1$ μs in all three materials (figures 9(a)–(c)). The proximity of the hotspots to the threshold line is quantified using the ignition risk factor (R) in equation (15). The results are shown in figure 9(d) that incorporates observations from multiple statistically similar instantiations for each material. Overall, the density of hotspots with a risk factor value of 1 is the highest in the PBX, followed by the soft MMX, and the hard MMX has the lowest risk profile among the three materials.

3.1.3. Probabilistic ignition behavior and time to criticality. Construction of probability distribution curves for ignition, based on the 'go'/'no-go' analysis (Barua *et al* 2013b) performed on statistically similar sample sets, takes into account the microstructural stochasticity involved in a material's ignition response. In addition, it also enables us to determine the median time to criticality and threshold loading velocity which serve as measures for the propensity of a material for ignition. For a piston velocity of 200 m s^{-1}, neither MMX shows any instance of ignition. On the contrary, instances of ignition exist for

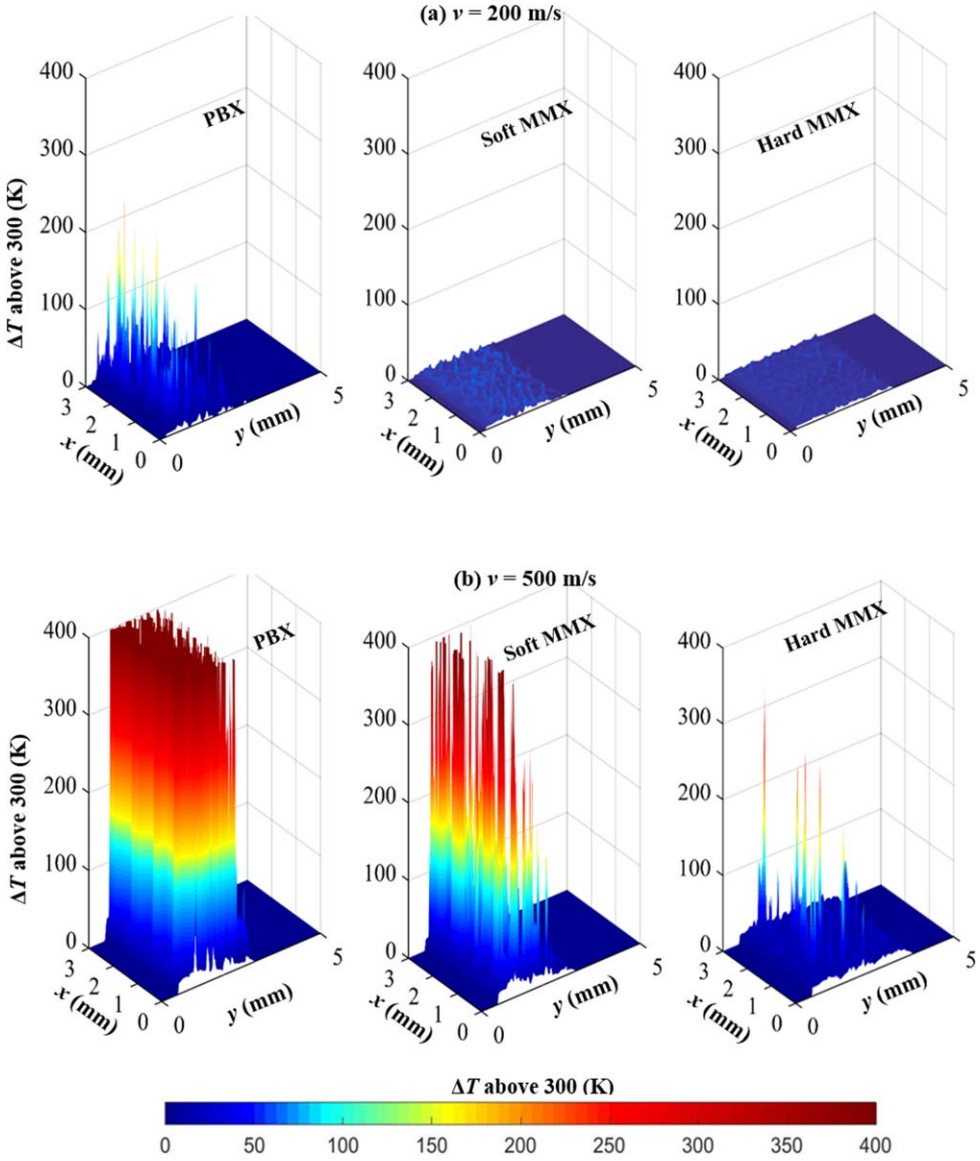

Figure 7. Distributions of temperature in PBX, soft MMX, and hard MMX after 1 μs of loading at (a) $v = 200\ \mathrm{m\,s^{-1}}$, and (b) $v = 500\ \mathrm{m\,s^{-1}}$.

the PBX, with the probability of ignition rising from 0 to 1 during the period of 1.5–2.22 μs after loading. At higher levels of piston velocity, the MMXs begin to show some instances of ignition. For a piston velocity of $500\ \mathrm{m\,s^{-1}}$, the probability distributions for ignition of the PBX, soft MMX, and hard MMX are depicted in figure 10(a). The values of t_0 (equation (16)) as indicated in the figure delineates the fact that the PBX undergoes ignition much earlier than the soft MMX, and the soft MMX undergoes ignition earlier than the hard MMX. The well-known 3-parameter Weibull distribution functions (equation (16)) are fitted to the curves of cumulative probability of ignition. The parameters (τ, m, and t_0) for PBX, soft MMX, and

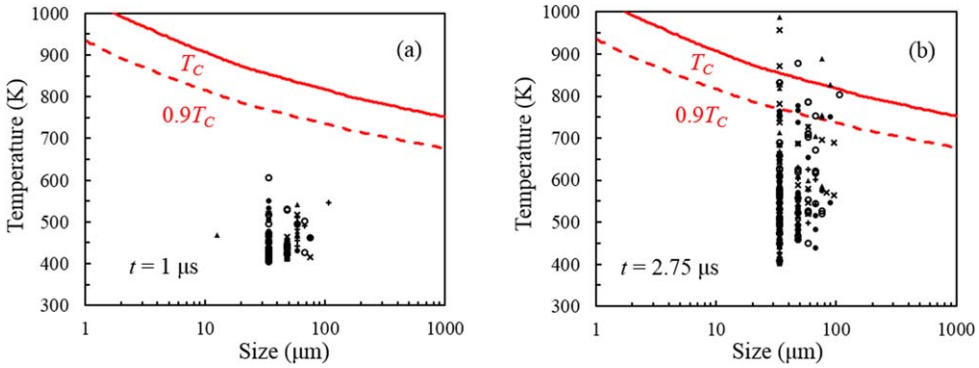

Figure 8. The size–temperature states of hotspots in PBX relative to the ignition threshold (T_C) of Tarver *et al* (1996) at (a) $t = 1$ μs, and (b) $t = 2.75$ μs. The loading velocity is 200 m s^{-1}. Different symbols on the plots correspond to five statistically similar instantiations of the PBX.

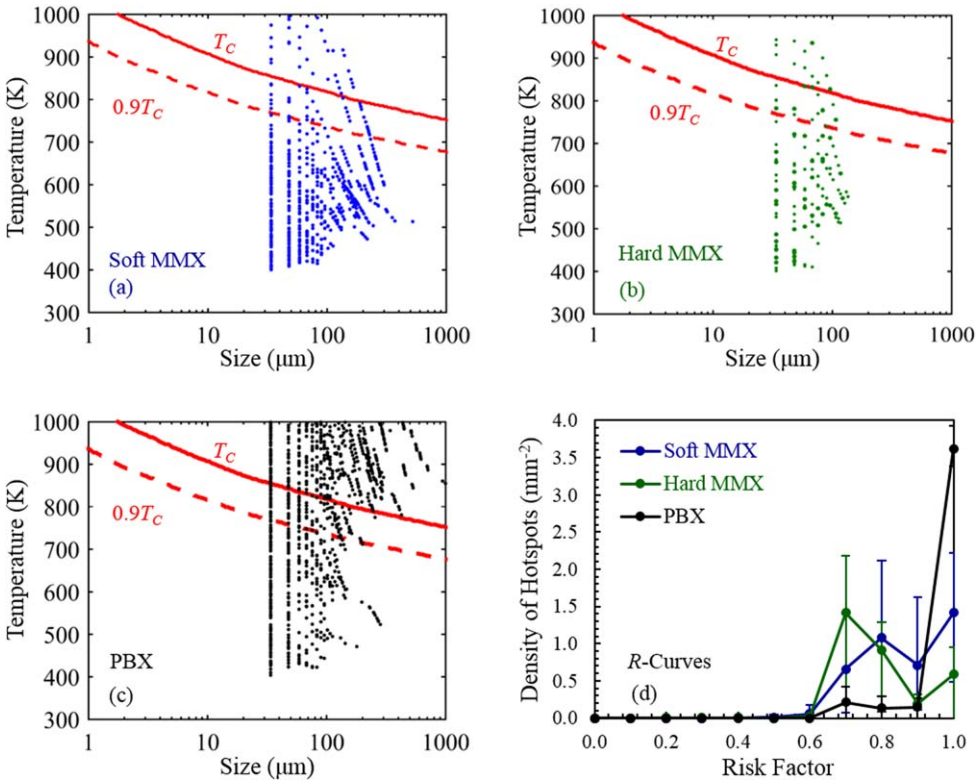

Figure 9. (a)–(c) The size–temperature state of hotspots in soft MMX, hard MMX, and PBX respectively, relative to the ignition threshold (T_C) of Tarver *et al* (1996), and (d) shows the density of hotspots with different values of the risk factor (R). The error bars indicate degree of variations among multiple samples in each material set. The results are for $v = 500$ m s^{-1} at $t = 1$ μs.

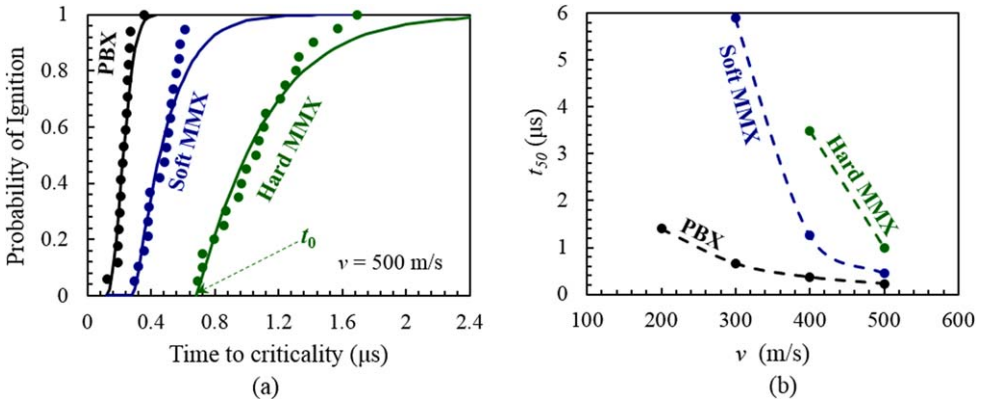

Figure 10. (a) Probability distribution of time to criticality determined from statistically similar sample sets of PBX, soft MMX, and hard MMX subjected to loading with an imposed piston velocity of 500 m s^{-1}. The lines are fits to the three-parameter Weibull probability distribution function. (b) Median time to criticality (t_{50}) as a function of loading velocity (v).

Table 5. Weibull distribution parameters for PBX, soft and hard MMX at $v = 500$ m s^{-1}.

Parameters	PBX	Soft MMX	Hard MMX
t_0 (μs)	0.12	0.29	0.68
τ	0.13	0.22	0.44
m	2.07	1.16	1.10
t_{50} (μs)	0.23	0.45	1.00

hard MMX are shown in table 5. The shape factor (m) is 2.07, 1.16, and 1.10 for the PBX, soft MMX, and hard MMX, respectively. These values indicate that the rate of increase of the probability of ignition is much higher for the PBX than those for the MMXs. The median time to ignition (t_{50}) is computed and plotted as a function of the loading velocity in figure 10(b). As the loading velocity increases, t_{50} decreases, indicating higher likelihood for ignition. At lower levels of piston velocity (<400 m s^{-1}), the probabilities of ignition for the soft and hard MMX are significantly lower than that for the PBX. The t_{50} values for the MMXs and the PBX are closer to each other as the piston velocity increases to 500 m s^{-1}.

3.1.4. Threshold velocity for ignition. As described by Barua *et al* (2013b), the variation of the scale factor τ with loading velocity can be used to estimate the critical velocity (v_c) below which no ignition occurs (probability of ignition = 0). τ influences the overall slope (and spread) of the probability distribution curve for ignition as in figure 10(a). For all three materials, τ decreases, or in other words, $(1/\tau)$ increases as the loading velocity increases. A lower value of $(1/\tau)$ corresponds to a wider spread of the probability distribution and hence a delay in reaching 50% probability of ignition, resulting in a higher value of t_{50}. The value of t_{50} tends to infinity as the value of $(1/\tau)$ tends to 0, indicating the threshold for ignition. Therefore, the value of $1/\tau$ for all materials is plotted as a function of loading velocity, and the resulting curves are extrapolated to $(1/\tau) = 0$. The values of v_c so obtained for the PBX, soft MMX, and hard MMX are 120, 230, and 374 m s^{-1}, respectively, as shown in figure 11.

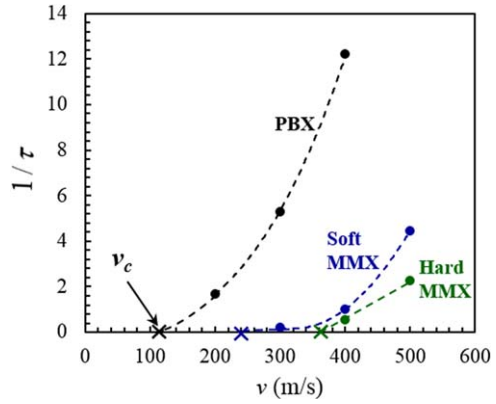

Figure 11. Time scale parameter (τ) in the Weibull probability distribution as a function of loading velocity (v) for the three materials. The curve for each material is extrapolated to $1/\tau = 0$ to determine its threshold velocity (v_c) for ignition.

The result indicates that the hard MMX requires higher energy input to ignite in comparison with the other two materials.

3.2. Mechanical response

3.2.1. Stress. The profiles of axial stress (compressive) in all three materials under the same conditions of loading are compared. Figure 12(a) shows the distributions of this stress in PBX, soft MMX, and hard MMX after 1 μs of monotonic loading at an imposed velocity of 200 m s^{-1}. The overall level decreases significantly from hard MMX, to soft MMX, and to PBX. The Al alloys, being ~3 times stiffer and stronger than HMX, provide reinforcement to the HMX grains. In contrast, the Estane in the PBX is less stiff and has much lower flow stress levels than the HMX. As a consequence, the stress wave travels faster in the MMXs than in the PBX. At a piston velocity of 200 m s^{-1}, the average axial stress in the soft and the hard MMXs is ~74% and ~150% higher, respectively, than that in the PBX. At 500 m s^{-1}, the difference in magnitudes of the average axial stress between the soft MMX and the PBX decreases to ~25%. On the other hand, the average axial stress level in the hard MMX continues to be significantly higher (~80%) than that in the PBX.

If the axial stress in the PBX (and the HMX phase in it) is lower than those in the MMXs, what causes the PBX (and the HMX in it in particular) to have more damage and localized heating? The answer lies in the stress triaxiality factor or the differences between the principal stress components. Figure 13(a) shows the distributions of the hydrostatic stress in the PBX, soft MMX, and hard MMX after 1 μs of monotonic loading at an imposed velocity of 200 m s^{-1}. The hydrostatic stress (σ_h) is

$$\sigma_h = -p = \sigma_{ii} = \frac{1}{3}(\sigma_{11} + \sigma_{22} + \sigma_{33}), \tag{17}$$

where σ_{11}, σ_{22}, and σ_{33} are normal components of the Cauchy stress tensor in a Cartesian coordinate system; and summation is implied on the repeated index i. The magnitude of σ_h in the HMX grains is highest for the hard MMX, followed by the soft MMX, and then the PBX. The magnitude of σ_h in the matrix increases slightly from the PBX to the soft MMX and to the hard MMX. Figure 13(b) shows the distributions of the Mises equivalent stress

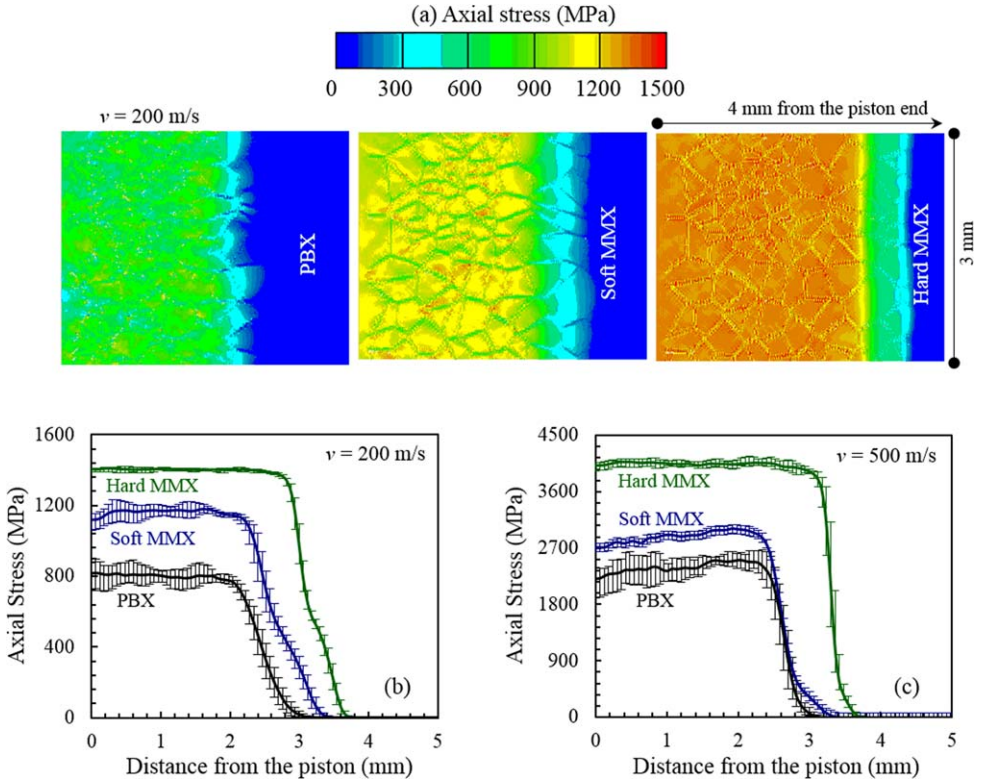

Figure 12. Distributions of axial stress in specimens of PBX, soft MMX, and hard MMX. (a) Axial stress contours for the imposed velocity of 200 m s^{-1}; (b) and (c) average axial stress along the loading direction for the imposed velocities of 200 and 500 m s^{-1} respectively. The error bars indicate ranges of variation among all samples in the corresponding sample set. All results correspond to $t = 1$ μs.

$$\overline{\sigma} = \sqrt{\frac{3}{2} s_{ij} s_{ij}} \tag{18}$$

in the PBX, soft MMX, and hard MMX after 1 μs of monotonic loading at an imposed velocity of 200 m s^{-1}. In the above expression, where $s_{ij}(i, j = 1 - 3)$ denote components of the deviatoric stress tensor. In the PBX, the magnitude of the Mises stress is very low in the Estane due to its viscoelastic constitutive response. In the soft MMX, the Mises stress in the 1100 Al alloy matrix is lower than that in the HMX grains. In contrast, the level of the Mises stress in the 7075 T651 Al alloy matrix is higher than that in the HMX grains in case of the hard MMX. The 7075 T651 Al alloy possesses a higher yield stress (527 MPa) than the HMX (yield stress = 260 MPa), whereas the 1100 Al alloy has a lower yield stress (148 MPa) than the HMX. The differences in yield stress of HMX and the Al alloys explain the distributions of the Mises stress in the MMXs. The magnitude of the Mises stress in the HMX grains increases slightly from the PBX to the soft MMX and to the hard MMX. The states of the average normal stress and the shear stress, in terms of the hydrostatic stress and the Mises stress, respectively, show that the overall states of stress in the grains are markedly different from that in the matrices. In addition, the states of stress vary significantly from one material to the other. To help delineate the trend, the stress triaxiality factor

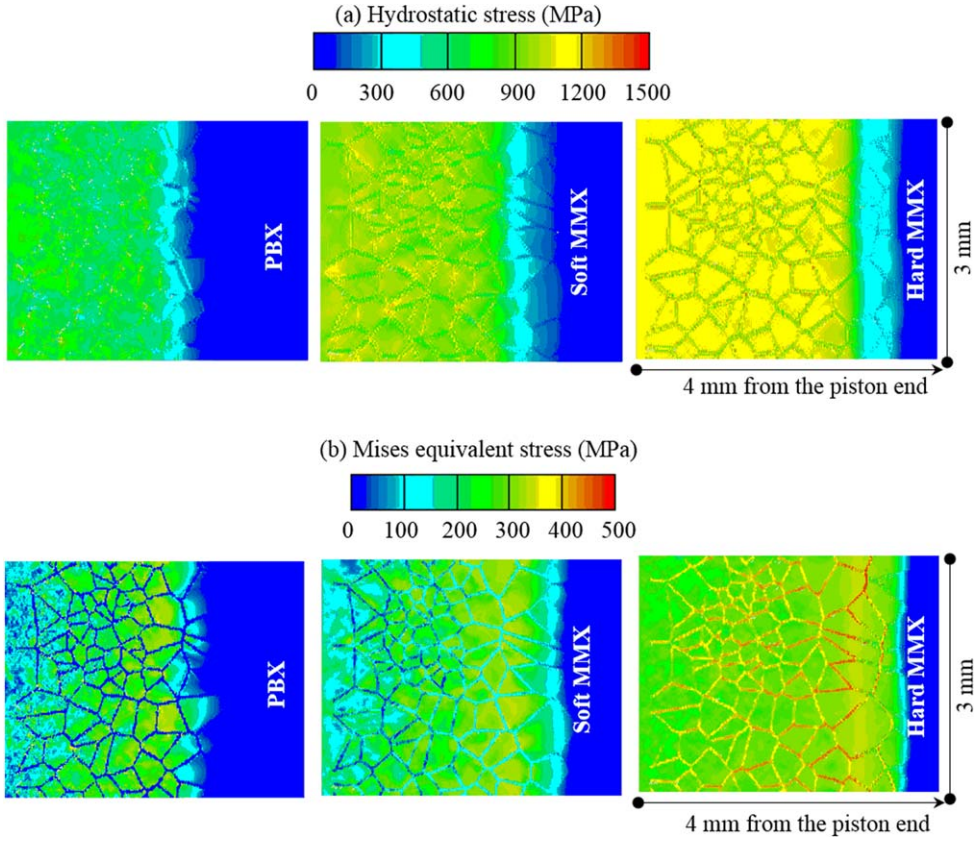

Figure 13. Distributions of (a) hydrostatic stress and (b) Mises equivalent stress in specimens of PBX, soft MMX, and hard MMX. All results correspond to $v = 200\ \mathrm{m\,s^{-1}}$, and $t = 1\ \mu\mathrm{s}$.

$$q = \frac{p}{\overline{\sigma}} \tag{19}$$

is plotted in figure 14(a). The results for the three materials are for 1 μs after loading at a velocity of 200 m s^{-1}. For the PBX and soft MMX, the stress triaxiality factor in the matrix is higher than that in the grains. However, in the hard MMX, the stress triaxiality factor is higher in the grains than in the matrix. Figures 14(b) and (c) compare q in the grains and the matrices in figure 14(a). Overall, the value in the HMX grains (of direct concern with regard to deformation, failure, and ignition) is highest in the hard MMX, followed by the soft MMX, and then the PBX (figure 14(b)). The opposite trend is seen in the matrices of the three materials (figure 14(c)). At higher loading intensities (not shown), the differences are even higher. Higher stress triaxiality values mean higher normal stress to shear stress ratios on potential crack faces or crack faces, and consequently lower likelihood for shear crack failure and lower frictional sliding on crack faces. This trend can be seen clearly by a look at the fracture behavior of the materials.

3.2.2. Crack distributions. The CFEM framework adopted here allows the nucleation and propagation of cracks in the microstructures to be explicitly tracked. For each material, three sets of parameters are used to describe the constitutive behavior of the interfaces and cracks,

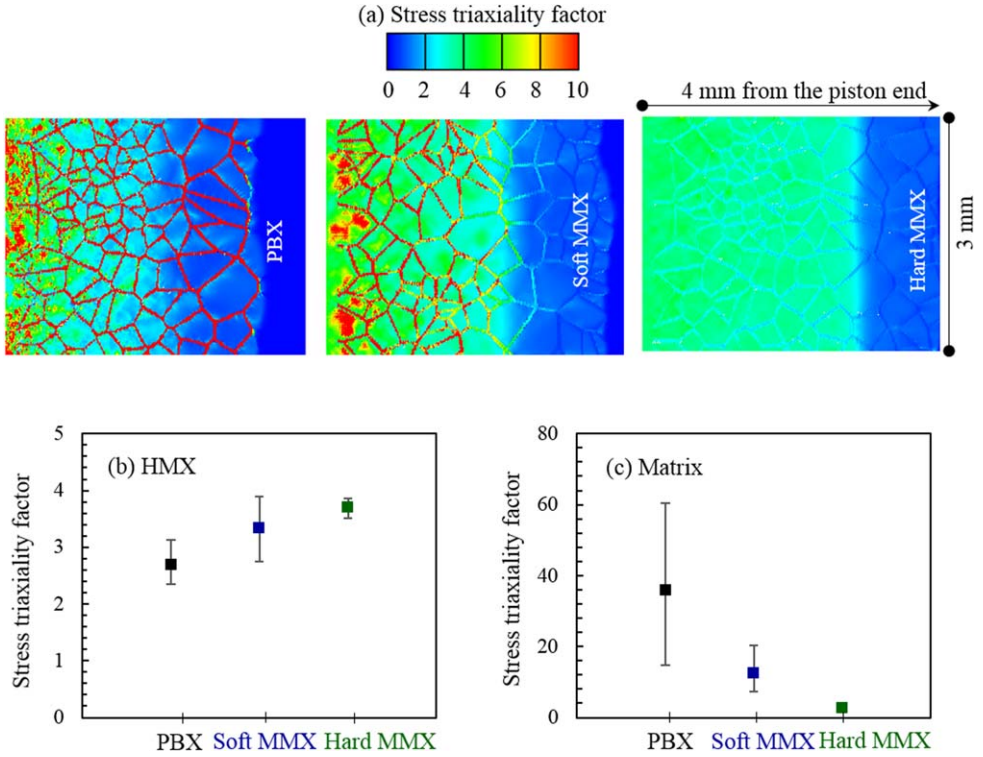

Figure 14. (a) Distributions of stress triaxiality factors in specimens of PBX, soft MMX, and hard MMX. Stress triaxiality factors in (b) the HMX grains and (c) the matrices in specimens of PBX, soft MMX, and hard MMX. The error bars indicate ranges of variation among all samples in the corresponding sample set. All results correspond to $v = 200\,\mathrm{m\,s^{-1}}$, and $t = 1\,\mu\mathrm{s}$.

one set for those inside the HMX grains, one set for those inside the matrix, and one set for the grain-matrix interfaces. Fracture along all possible types of sites is considered. The behaviors of the three types of fracture are analyzed in figure 15 using crack density, or crack length per unit area of the material, after 1 μs of loading as a function of piston velocity. The crack density in the PBX (figure 15(a)) is significantly higher than that in the soft MMX (figure 15(b)). All three types of fracture are seen in the PBX, while only grain fracture is seen in the soft MMX. In particular, at a piston velocity of $200\,\mathrm{m\,s^{-1}}$, the crack densities in the Estane matrix and the HMX grains are comparable, while the crack density associated with the interfaces is approximately twice as high. At piston velocities above $400\,\mathrm{m\,s^{-1}}$, however, fracture in the grains dominates. For the soft MMX (figure 15(b)) and hard MMX (not shown), fracture in the grains is the only mode of damage observed. Specifically, matrix fracture and grain/matrix fracture are negligible in the soft MMX (figure 15(b)) and even less fracture is observed in the hard MMX in general. In the hard MMX, few intragranular cracks are seen even at velocities higher than $400\,\mathrm{m\,s^{-1}}$. Overall, the crack densities in the hard MMX are one to two orders of magnitude lower than those in the PBX. In general, the crack density is higher near the loading site (the piston end), as is evident from figure 16(a). The overall intragranular crack density for the hard MMX shows little increase as the load

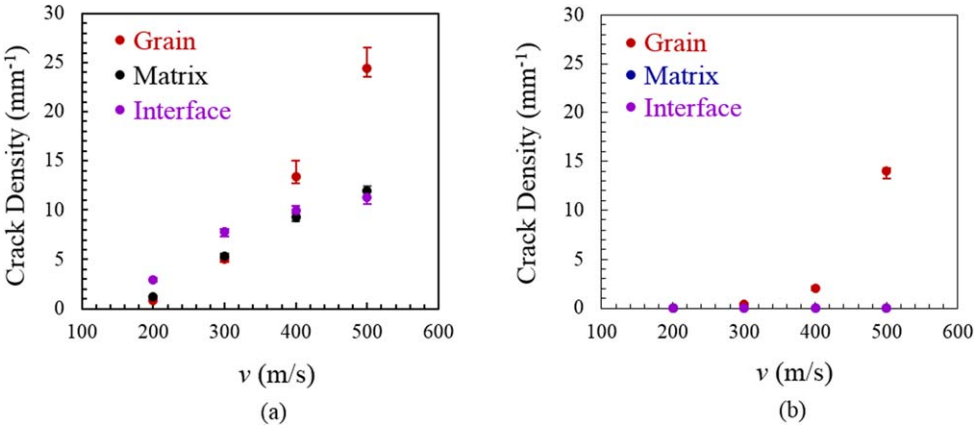

Figure 15. Crack density in grain and matrix and along grain-matrix interface as a function of impact velocity (v) in (a) PBX and (b) soft MMX after 1 μs of loading. The crack density for the hard MMX is one to two orders of magnitude lower than what is shown here.

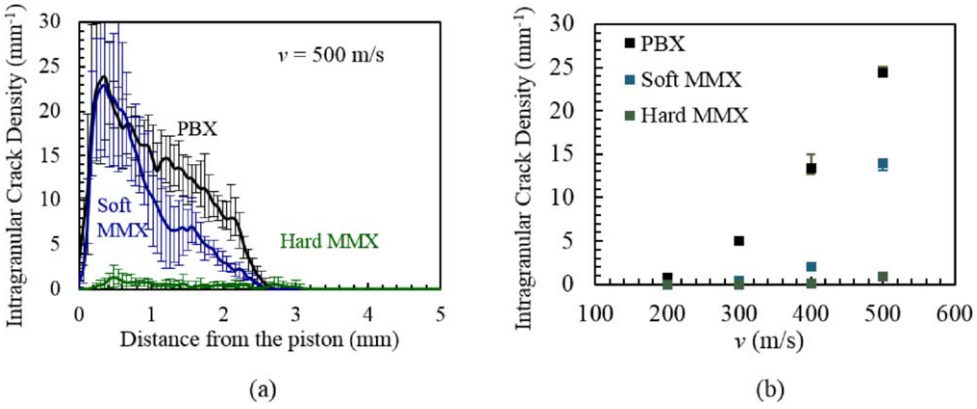

Figure 16. A comparison of the intragranular crack density as a function of (a) the distance from the loading site and (b) the imposed impact velocity (v) for PBX, soft MMX, and hard MMX. All results correspond to $t = 1$ μs.

intensity (piston velocity) increases, in contrast to what is seen for the PBX and the soft MMX (figure 16(b)).

The differences in fracture behavior seen here are a direct result of the load triaxiality differences observed in figure 14. Due to the compressive nature of the loading, failure along potential fracture sites is primarily governed by shear separation rather than normal separation. The extent of damage is highest in the PBX, followed by the soft MMX, and then the hard MMX. The stress triaxiality factors and fracture toughness of the microstructural constituents explain the damage behavior of the three EMs. The stress triaxiality factor in the grains is lowest in the PBX, followed by the soft MMX, and then the hard MMX. For the matrices, the very low fracture toughness of Estane (0.25 MPa$\sqrt{\text{m}}$) causes to experience extensive failure despite a relatively high stress triaxiality factor. In contrast, the Al alloys in the MMXs have much higher fracture toughness levels (15–24 MPa$\sqrt{\text{m}}$). The disparity in

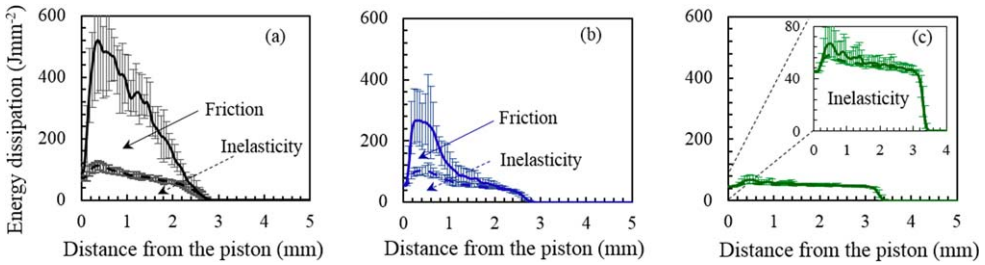

Figure 17. Distributions of the total energy dissipation as a function of the distance from the loading site for (a) PBX, (b) soft MMX, and (c) hard MMX. The area under the dotted curve indicates the fraction of the total energy dissipated due to inelastic deformation. The remaining area under the solid curve represents the energy dissipated due to friction. The results are for $v = 500\ \mathrm{m\,s^{-1}}$ and $t = 1\ \mu\mathrm{s}$.

stress triaxiality factors for the grains and the matrix is highest for the PBX, followed by the soft MMX, and then the hard MMX. This disparity increases as load intensity increases, leading to more damage. Cracks are more likely to initiate in and propagate from regions of low stress triaxiality to regions of high stress triaxiality.

3.2.3. Energy dissipation. Energy dissipation due to friction along fracture surfaces and inelastic deformation (elastic-viscoplastic, viscoelastic) of the constituents in the microstructures is responsible for the heating that leads to the hotspots. Figure 17 shows the energy dissipation in the three materials. The dissipation levels for all three materials at $200\ \mathrm{m\,s^{-1}}$ are quite low, so only results for $500\ \mathrm{m\,s^{-1}}$ are shown. The PBX has the highest level of dissipation in terms of the total (including contributions from friction and bulk inelasticity), followed by the soft MMX, and then by the hard MMX. The dissipation due to bulk inelasticity is distributed over most of the material traversed by the stress wave. In contrast, frictional dissipation gravitates toward the loading site for the PBX and the soft MMX. For the PBX, frictional dissipation dominates, as it shows the most extensive fracture (figures 14 and 15). For the soft MMX on the other end, the two forms of dissipation are comparable. The hard MMX does not show significant frictional heating, as no extensive fracture occurs in it as indicated earlier.

4. Discussion

The above results show that the thermo-mechanical response of the MMXs to monotonic impact is significantly different from that of the PBX. Figure 18 summarizes the correlation between the mechanical behavior and the ignition response in terms of median time to criticality over a range of load intensity. For a particular loading intensity, the value of t_{50} is lower (in other words, propensity for ignition is higher) for the material which exhibits lower levels of average axial stress (figure 18(a)) and higher levels of damage (figure 18(b)). This ostensibly counter-intuitive observation is explained in terms of the stress triaxiality factor, as stated earlier. As it turns out, the material (PBX) with lower levels of axial stress has lower levels of stress triaxiality which result in more shear fracture and internal crack face friction. More damage and frictional heating lead to higher propensity for ignition through hotspot generation. The Al alloy matrices in the MMXs have higher stiffness and fracture resistance levels than Estane and HMX. As a result, the MMXs can sustain higher load intensities and

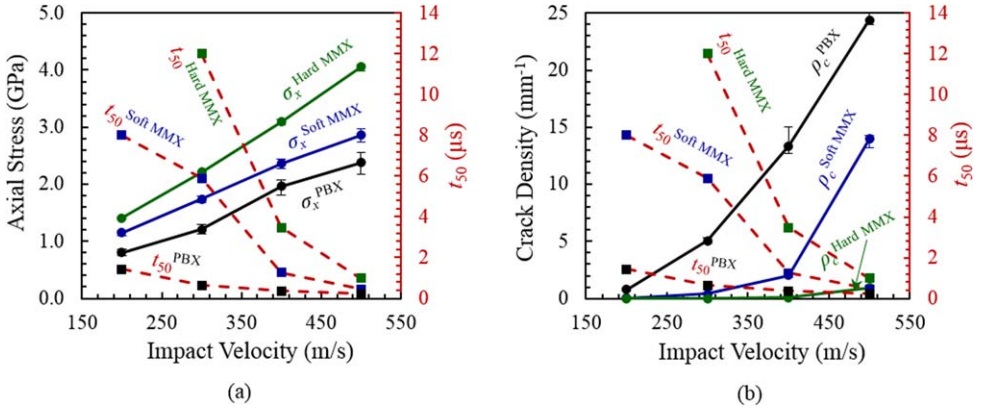

Figure 18. Correlation between the median time to criticality (t_{50}) and (a) the axial stress (σ_x) and (b) the crack density (ρ_c) at an instant of 1 μs, at different impact velocities.

experience lower levels of damage compared with the PBX. The material having the strongest and toughest matrix (7075 T651 Al alloy) shows the highest failure resistance and lowest propensity for heating.

For the MMXs, the dominant mode of energy dissipation is bulk viscoplasticity, which is spread more widely in the material and less localized. This is another reason why the MMXs experience much less intense localized heating relative to the PBX. The outcome of the influences of all these factors is that the minimum piston velocities required for ignition for the hard MMX and soft MMX are ~3 times and ~2 times that for the PBX, respectively. This implies that a stronger and tougher viscoplastic matrix increases the threshold velocity for ignition. Thus, the reinforcement of energetic grains through stronger and tougher viscoplastic matrix strongly influences the overall performance of the energetic system, and the influence is more pronounced at lower load intensities than at higher intensities. The magnitudes of threshold velocity for ignition and the comparative study of different materials can be the performance metric for experimental validation in the future.

The analyses carried out here represent a parametric study based on available data on existing materials, including HMX, Estane, and two commercial grade Al alloys. It is worth mentioning that the computational framework adopted here has been validated with experimental observations and reported in earlier publications (Barua and Zhou 2011a, Hardin 2015, Kim *et al* 2016). Barua *et al* compared measured and calculated $\sigma-\varepsilon$ responses of PBX 9501 subjected to uniaxial compression at three initial temperatures from 233 and 290 K, at a strain rate of $\dot{\varepsilon} = 2500\,\mathrm{s}^{-1}$. Figure 10 from Barua and Zhou (2011b) shows that the calculated and measured responses are in good agreement. Hardin calibrated the elastic-viscoplastic constitutive laws for HMX by matching calculated and measured Hugoniot relations between longitudinal stress and piston velocity (Hardin 2015). We use the same elastic-viscoplastic constitutive model for HMX here. Kim *et al* examined shock initiation threshold of pressed HMX, pure TATB and TATB/binder PBX using the same cohesive finite element framework (Kim *et al* 2016). Figure 15 of the Kim *et al* (2016) shows the James relation and figure 17 of the same reference shows the equivalent James relation and Walker–Wasley relation characterizations of the experimentally obtained ignition data. Figure 20 of Kim *et al* (2016) shows ignition probability distribution maps experimentally obtained for pressed granular HMX of different grain sizes and the ignition probability distribution

maps calculated using computationally generated statistically similar microstructure sets for the granular HMX. The trends in the two sets of maps match in all the cases. Li and Zhou adopted the same cohesive finite element approach to study fracture in a non-energetic Al_2O_3/TiB_2 composite system (Li and Zhou 2013). They predicted fracture toughness of the two-phase composite as function of microstructure and modeled the crack-particle interactions and the results compare well with experimental measurements. Thus, the computational framework adopted here has been extensively validated and verified for both energetic and non-energetic systems.

The soft MMX and the hard MMX have not been experimentally fabricated in the form analyzed. Because of this, the analyses reported here should be regarded as a materials design and exploration exercise which helps provide insight and guidance for development of new materials not yet in existence. Ultimately, such analyses can lead to new materials if and when the material configurations are realized in the laboratory via synthesis, evaporation or AM. As we pointed out at the outset of this paper, such an attempt is not made here. It is hoped that our analyses here will motivate and induce efforts in this regard. We also hope to report results of such an experimental project in the future.

5. Conclusions

This study can be regarded as a CMD and exploration attempt, as it concerns materials both in existence and not yet in existence. The thermo-mechanical response and ignition behavior of a PBX and two metal–matrix composite configurations (referred as MMXs, or metal–matrix explosives) under monotonic impact loading is analyzed using the Lagrangian cohesive finite element framework CODEX. The analyses focus on the deformation, failure, energy dissipation, and hotspot dynamics. The objective is to compare the ignition behaviors of these materials as existing or potential new designs of EMs. The three materials have the same microstructure configurations and energetic grains. This only difference between the materials is the type and properties of the matrix (or binders). The study yielded the following findings.

(1) The type and properties of the matrix of the HEMs significantly influence their response and ignition behavior. In particular, the critical impact velocity required for ignition is 120, 230, and 374 $m\,s^{-1}$ for the PBX, soft MMX, and hard MMX, respectively.
(2) A probabilistic analysis is carried using sets of multiple statistically equivalent microstructure samples. The time required to reach a 50% probability of ignition decreases as impact velocity or load intensity increases. The differences in median time to criticality among the MMXs and the PBX also decrease as the load intensity increases. At a given load intensity (impact velocity), the time required to reach a 50% probability of ignition is longest for the hard MMX, followed by the soft MMX, and then the PBX. This trend reflects the same rank order of localized heating due to frictional sliding along crack faces and bulk inelasticity in the materials.
(3) The viscoplastic metallic matrix (Al alloys in particular), with high fracture toughness levels, strengthens the energetic system and reduces damage. As a result, the MMXs show a lower extent of localized heating and therefore a lower propensity for ignition, as manifested through a higher critical loading velocity and a longer median time to criticality. Among the three EMs, the hard MMX, consisting of the strongest and toughest 7075 T651 Al alloy, shows the lowest propensity for ignition.

The above results reveal that replacing the Estane binder in the PBX with Al alloys can significantly lower the propensity for ignition and the mechanism stems from the fact that the

thermal-mechanical matching of the HMX grains and the Al alloys in the MMX reduce damage and localized heating in the energetic HMX grains. This understanding points out a potential avenue for desensitizing PBXs. The benefit of the metal–matrix explosives can go beyond lower impact sensitivity. In particular, the Al alloy based metallic matrices can also impart strength and toughness to the EMs, lead to better thermal stability at elevated temperatures, and lend the overall EMs to simultaneous, large-scale detonation by electric impulses via bridge wires. This is a computational study aimed at exploring potentially attractive material design that are not yet in existence. The understanding and insight can motivate efforts to develop such new materials. The study here should also be subject to experimental verification as such materials become a reality.

Acknowledgments

The authors gratefully acknowledge support from the Defense Threat Reduction Agency (DTRA) (Dr Allen Dalton) and the Air Force Office of Scientific Research (Dr Martin Schmidt). Calculations are carried out on parallel computers at DPRL at Georgia Tech and on supercomputers at MSRCs through the DoD HPCMP.

ORCID iDs

Min Zhou https://orcid.org/0000-0002-8993-5675

References

Ahmad J F and Alkammash I Y 2012 Theoretical study of some thermodynamical properties for solid under high pressure using finite-strain EOS *J. Assoc. Arab Univ. Basic Appl. Sci.* **12** 17–22

Asay B 2010 *Non-Shock Initiation of Explosives* (Berlin: Springer)

Baer M R 2002 Modeling heterogeneous energetic materials at the mesoscale *Thermochim. Acta* **384** 351–67

Barua A 2013 Mesoscale computational prediction and quantification of thermomechanical ignition behavior of polymer-bonded explosives (PBXs) *PhD Thesis* Georgia Institute of Technology

Barua A, Horie Y and Zhou M 2012a Energy localization in HMX-Estane polymer-bonded explosives during impact loading *J. Appl. Phys.* **111** 054902

Barua A, Horie Y and Zhou M 2012b Microstructural level response of HMX-Estane polymer-bonded explosive under effects of transient stress waves *Proc. R. Soc.* A **468** 3725–44

Barua A, Kim S, Horie Y and Zhou M 2013a Ignition criterion for heterogeneous energetic materials based on hotspot size–temperature threshold *J. Appl. Phys.* **113** 064906

Barua A, Kim S, Horie Y and Zhou M 2013b Prediction of probabilistic ignition behavior of polymer-bonded explosives from microstructural stochasticity *J. Appl. Phys.* **113** 184907

Barua A and Zhou M 2011a A framework for analyzing the microstructure level thermomechanical response of polymer bonded explosives *Mater. Sci. Forum* **673** 21–33

Barua A and Zhou M 2011b A Lagrangian framework for analyzing microstructural level response of polymer-bonded explosives *Modelling Simul. Mater. Sci. Eng.* **19** 055001

Brar N S, Joshi V S and Harris B W 2009 Constitutive model constants for Al7075-T651 and Al7075-T6 *AIP Conf. Proc.* **1195** 945–8

Brousseau P, Dorsett H E, Cliff M D and Anderson C J 2002 Detonation properties of explosives containing nanometric aluminum powder *Proc. 12th Int. Detonation Symp. (San Diego, CA, 12–16 August 2002)* pp 11–21

Chidester S, Green L and Lee C 1993 A frictional work predictive method for the initiation of solid high explosives from low-pressure impacts *Tenth Int. Detonation Symp.*

Dahmen H V 1904 *US Patent* US770046A

Daniel A M 2006 *Polyurethane Binder Systems for Polymer Bonded Explosives* ADA467800 Weapon Systems Division: Defense Science and Technology Organization
Dick J J, Hooks D E, Menikoff R and Martinez A R 2004 Elastic-plastic wave profiles in cyclotetramethylene tetranitramine crystals *J. Appl. Phys.* **96** 374–9
Dickson P, Parker G, Smilowitz L, Zucker J and Asay B 2006 Frictional heating and ignition of energetic materials *AIP Conf. Proc.* **845** 1057–60
Foster J C Jr, Stewart D S and Thomas K 2007 Multi-scale statistical design of high energy density materials *AIP Conf. Proc.* **955** 369
Ghosh S, Nowak Z and Lee K 1997 Quantitative characterization and modeling of composite microstructures by Voronoi cells *Acta Mater.* **45** 2215–34
Gilbert J and Gonthier K 2012 Meso-scale computation of uniaxial waves in granular explosives-analysis of deformation induced ignition *50th AIAA Aerospace Sciences Meeting including the New Horizons Forum and Aerospace Exposition* (American Institute of Aeronautics and Astronautics)
Gonthier K A 2003 Modeling and analysis of reactive compaction for granular energetic solids *Combust. Sci. Technol.* **175** 1679–709
Green L, Weston A and Van Velkinburg J 1971 *Mechanical and Frictional Behavior of Skid Test Hemispherical Billets* UCRL-51085 Lawrence Livermore National Laboratory
Guo N and Leu M C 2013 Additive manufacturing: technology, applications and research needs *Frontiers Mech. Eng.* **8** 215–43
Hardin D B 2015 The role of viscoplasticity in the deformation and ignition response of polymer bonded explosives *PhD Thesis* Georgia Institute of Technology
Horie Y 2014 Hot spots, high explosives ignition, and material microstructure *Mater. Sci. Forum* **767** 3–12
Hudson R J, Zioupos P and Gill P P 2012 Investigating the mechanical properties of RDX crystals using nano-indentation *Propellants, Explosives, Pyrotechnics* **37** 191–7
Iqbal M A, Gupta G and Gupta N K 2010 3D numerical simulations of ductile targets subjected to oblique impact by sharp nosed projectiles *Int. J. Solids Struct.* **47** 224–37
Kim S, Horie Y and Zhou M 2014 Ignition desensitization of PBX via aluminization *Metall. Mater. Trans.* A **46** 4578–86
Kim S, Miller C, Horie Y, Molek C, Welle E and Zhou M 2016 Computational prediction of probabilistic ignition threshold of pressed granular octahydro-1,3,5,7-tetranitro-1,2,3,5-tetrazocine (HMX) under shock loading *J. Appl. Phys.* **120** 115902
Landerville A C, Conroy M W, Budzevich M M, Lin Y, White C T and Oleynik I I 2010 Equations of state for energetic materials from density functional theory with van der Waals, thermal, and zero-point energy corrections *Appl. Phys. Lett.* **97** 251908
Lewis J A 2006 Direct ink writing of 3D functional materials *Adv. Funct. Mater.* **16** 2193–204
Li Y and Zhou M 2013 Prediction of fracture toughness of ceramic composites as function of microstructure: I. Numerical simulations *J. Mech. Phys. Solids* **61** 472–88
Panchadhara R and Gonthier K A 2011 Mesoscale analysis of volumetric and surface dissipation in granular explosive induced by uniaxial deformation waves *Shock Waves* **21** 43–61
Prakash V, Sinha R K and Singh H 2004 *Def. Sci. J.* **54** 475–82
Radwan M 2001 Explosive characteristics of aluminized PBXs based on HMX and polyurethane binder *32nd Int. Annual Conf. of ICT (Karlsruhe, Germany)* p 44
Rai N K, Schmidt M J and Udaykumar H 2017a Collapse of elongated voids in porous energetic materials: effects of void orientation and aspect ratio on initiation *Phys. Rev. Fluids* **2** 043201
Rai N K, Schmidt M J and Udaykumar H 2017b High-resolution simulations of cylindrical void collapse in energetic materials: effect of primary and secondary collapse on initiation thresholds *Phys. Rev. Fluids* **2** 043202
Rumchik C G, Jordan J L, Elert M, Furnish M D, Chau R, Holmes N and Nguyen J 2007 Effect of aluminum particle size on the high strain rate properties of pressed aluminized explosives *AIP Conf. Proc.* **955** 795–8
Ruzz-Nuglo F D 2014 *AIAA Propulsion and Energy Forum*
Schrand A 2016 Additive manufacturing: from form to function *Strateg. Stud. Q.* **10** 74
Tarver C M, Chidester S K and Nichols A L 1996 Critical conditions for impact- and shock-induced hot spots in solid explosives *J. Phys. Chem.* **100** 5794–9
Tarver C M and Tran T D 2004 Thermal decomposition models for HMX-based plastic bonded explosives *Combust. Flame* **137** 50–62

Trott W M, Baer M R, Castaneda J N, Chhabildas L C and Asay J R 2007 Investigation of the mesoscopic scale response of low-density pressings of granular sugar under impact *J. Appl. Phys.* **101** 024917

Trzciński W A, Cudziło S and Szymańczyk L 2007 Studies of detonation characteristics of aluminum enriched RDX compositions *Propellants, Explosives, Pyrotechnics* **32** 392–400

Vadhe P P, Sinha R K, Pawar R B, Asthana S N and Rao A S 2008 Cast aluminized explosives (review) *Combust., Explosion, Shock Waves* **44** 461–77

Zhai J, Tomar V and Zhou M 2004 Micromechanical simulation of dynamic fracture using the cohesive finite element method *J. Eng. Mater. Technol.* **126** 179–91

Zhou M, Needleman A and Clifton R J 1994 Finite-element simulations of shear localization in plate impact *J. Mech. Phys. Solids* **42** 423–58